Energy Storage Materials 38 (2021) 80–92

Contents lists available at ScienceDirect

Energy Storage Materials

journal homepage: www.elsevier.com/locate/ensm

Insight on electrolyte infiltration of lithium ion battery electrodes by means of a new three-dimensional-resolved lattice Boltzmann model

Abbos Shodiev[a,b], Emiliano Primo[a,b], Oier Arcelus[a,b], Mehdi Chouchane[a,b], Markus Osenberg[c], André Hilger[c], Ingo Manke[c], Jianlin Li[d], Alejandro A. Franco[a,b,e,f,*]

[a] Laboratoire de Réactivité et Chimie des Solides (LRCS), UMR CNRS 7314, Université de Picardie Jules Verne, Hub de l'Energie, 15 rue Baudelocque, 80039 Amiens Cedex, France
[b] Réseau sur le Stockage Electrochimique de l'Energie (RS2E), Fédération de Recherche CNRS 3459, Hub de l'Energie, 15 rue Baudelocque, 80039 Amiens Cedex, France
[c] Institute of Applied Materials, Helmholtz-Zentrum Berlin für Materialien und Energie GmbH, Hahn-Meitner-Platz 1, 14109, Berlin, Germany
[d] Electrification and Energy Infrastructure Division, Oak Ridge National Laboratory, Oak Ridge, TN, 37831 USA
[e] ALISTORE-European Research Institute, Fédération de Recherche CNRS 3104, Hub de l'Energie, 15 rue Baudelocque, 80039 Amiens Cedex, France
[f] Institut Universitaire de France, 103 Boulevard Saint Michel, 75005 Paris, France

ARTICLE INFO

KEYWORDS:
Li-ion batteries
Manufacturing process
Electrolyte filling
Lattice Boltzmann modeling
Fluid dynamics

ABSTRACT

Electrolyte filling takes place between sealing and formation in Lithium Ion Battery (LIB) manufacturing process. This step is crucial as it is directly linked to LIB quality and affects the subsequent time consuming electrolyte wetting process. Although having fast, homogeneous and complete wetting is of paramount importance, this process has not been sufficiently examined and fully understood. For instance, experimentally available data is insufficient to fully capture the complex interplay upon filling between electrolyte and air inside the porous electrode. We report here for the first time a 3D-resolved Lattice Boltzmann Method (LBM) model able to simulate electrolyte filling upon applied pressure of LIB porous electrodes obtained both from experiments (micro X-ray tomography) and computations (stochastic generation, simulation of the manufacturing process using Coarse Grained Molecular Dynamics and Discrete Element Method). The model allows obtaining advanced insights about the impact of the electrode mesostructures on the speed of electrolyte impregnation and wetting, highlighting the importance of porosity, pore size distribution and pores interconnectivity on the filling dynamics. Furthermore, we identify scenarios where volumes with trapped air (dead zones) appear and evaluate the impact of those on the electrochemical behavior of the electrodes.

Introduction

Lithium-ion batteries (LIBs) are widely used as energy storage devices in electronic gadgets, electric vehicles, and stationary applications; due to their high power and energy densities, and good cycle life [1]. As the urge to shift to environment-friendly technologies is rising, the demand for LIBs is aggressively increasing not only within these domains but also across many other areas. Consequently, decreasing LIBs cost becomes one of the most critical barriers to overcome. Alongside the massive improvement in cell chemistry, [2] it is critical to optimize the manufacturing process in order to improve its quality: one of its bottleneck steps is to ensure homogenous electrolyte impregnation within the electrode porous mesostructure [3-6]. There are several specific technical reasons behind this claim. Firstly, the electrolyte wetting of LIB cells takes a relatively longer time than other steps during manufacturing [4]. Secondly, since the charge transfer occurs at the electrolyte-electrode interface, the electrolyte infiltration determines the total electrochemically active surface area and, therefore, the cell energy and power capability [7–9]. Moreover, incomplete wetting can create "dead electrode zones" which may potentially lead to the formation of dendrites, inducing short circuits and reducing the battery cycle life [3,10,11].

Davoodabadi *et al.* performed quantitative wettability measurements on NMC532-based cathodes, identifying two important parameters: the electrolyte penetrance coefficient and the solid permeability coefficient [5]. They found that the electrolyte with a greater value of the former wets faster the electrode, whereas the electrode with a greater value of the latter is more amenable to impregnation. Furthermore, studies performed by the same group revealed that the calendering degree (*i.e.,* the porosity of the electrode after the calendering), the wetting temperature, the nature of the solvent used to prepare the electrode slurry (*i.e.,* organic vs. aqueous) and the concentration of the electrolyte's salt play a key role in the wetting rate [10]. A ceramic coating on separator also improved the electrolyte wetting on the in-plane direction [12]. Günter *et al.* studied the impact of the amount of electrolyte on the performance

* Corresponding author
E-mail address: alejandro.franco@u-picardie.fr (A.A. Franco).

https://doi.org/10.1016/j.ensm.2021.02.029
Received 18 December 2020; Received in revised form 27 January 2021; Accepted 19 February 2021
Available online 24 February 2021

of large-format LIB cells [13]. They analyzed the filling and the formation process and performed cyclability tests, finding interdependencies between the electrolyte quantity, the wetting rate, the cell capacity, and energy density. Working also with large-format LIB cells, Weydanz *et al.* used neutron imaging to visualize in real-time the electrolyte impregnation and analyzed the effect of using vacuum to reduce the wetting time [14]. It was also demonstrated that the electrode surface morphology, the separator material and the interphase between them affect the wetting kinetics [15-17].

Despite the importance of the topic, reliable and broad scientific data does not exist in the literature [3], [18]. There are several patent reports and scientific publications, but nevertheless, the electrode wetting process has not been sufficiently explored [4]. Electrolyte wetting has been evaluated experimentally by wetting balance and 2D in-plane imbibition methods. However, the experimental results cannot provide any information on how and what portion of the pores were filled [5]. The visualization favors a straightforward understanding of its profound nature [5],[11],[18]. However, it is a challenging task from an experimental perspective. The components of the cells, such as electrodes, separators, and housing, are not transparent to visible light. Furthermore, the vacuum chamber, where usually the electrodes are filled, does not allow doing *in situ* experiments. To the best of our knowledge, only a few papers report the visualization of the liquid penetration by using transmission neutron and X-ray imaging [18],[19],[20]. These studies did not have the appropriate resolution to provide detailed information on how the pores were filled with electrolyte during the whole process, due to the limitations of the techniques.

Another path to address this puzzle is the utilization of computational methods to simulate porous media flow. Computational fluid dynamics based on finite element method (FEM) and finite volume methods (FVM) have been the most dominant tools to solve fluid dynamics problems [21]. Nevertheless, they cannot be applied in a straightforward way to 3D-resolved porous media phenomena where boundaries are complex and involve biphasic (gas/liquid) interface dynamics [11,22]. Recently, the increase in computational power and the development of the so-called Lattice Boltzmann Method (LBM) made possible to describe this process meticulously [22–24]. Compared to other techniques, the strength of the LBM is its mesoscopic nature based on the discrete kinetic theory. At the mesoscopic level, the LBM models combine microscopic dynamics, such as fluid-fluid and fluid-solid boundary interactions, and the macroscopic kinetic theory of fluids, like the Navier-Stokes equation for the bulk flow [25]. Moreover, several multiphase models reported recently advanced its capacity to simulate multiphase flow, becoming very attractive [26]. In spite of its advantages, LBM is a new tool, and few codes were developed compared to traditional computational fluid dynamics (CFD) methods [26]. Furthermore, LBM is computationally very expensive, which limits its deployment to an efficient and parallel usage of supercomputers [11,27]. Regardless these difficulties, Lee et al. implemented LBM to characterize electrolyte transport in the porous LIB electrode [11,27]. Despite the successful utilization and essential insights from the study, the model was only two dimensional, and flow was limited in some directions. Their simulation was based on an ideal case where only active material particles with perfectly spherical shape were considered. Furthermore, the inactive components, such as conductive additive and binder, which are known to significantly impact the AM active surface and pores structure, [11,20,27] were not explicitly considered. Hence further studies on three-dimensional models are required to capture the full picture of the process.

For the first time, this study reports insights about the electrolyte filling dynamics in electrodes with three-dimensional resolution based on an innovative Lattice Boltzmann model where realistic geometries of electrodes were utilized. Furthermore, the impact of electrode porosity on electrolyte wetting dynamics was explored using electrodes generated by stochastic simulations, tomography characterizations and by the simulation of the electrodes manufacturing process. The separator's role and its surface contact with the electrode on electrolyte penetration was also characterized, and the electrolyte penetration was simulated in a full 3D LIB cell.

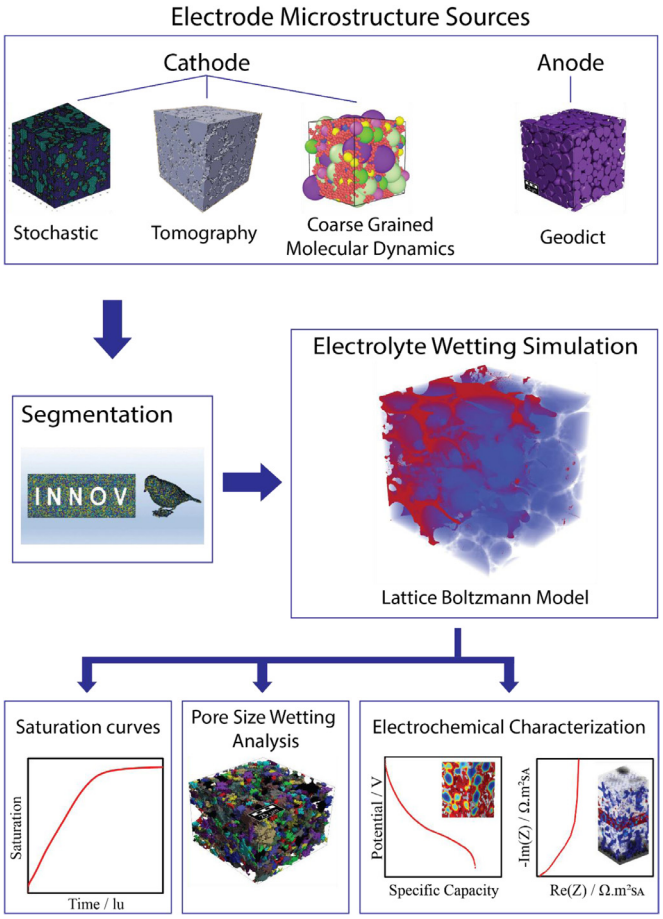

Figure 1. Schematic representation of the workflow used in the LBM simulation and its subsequent analysis.

2. Workflow and model description

2.1. Workflow

The workflow of our study is summarized in Figure 1. Through LBM, the electrolyte impregnation simulations were performed over 3D electrode mesostructures of NMC-based cathodes and full LIB cell, including the graphite anode and the separator. The 3D NMC cathode mesostructures were generated through three different approaches. The first one is the stochastic generation by using our *in-house* INNOV code [28]. In short, spherical particles are placed randomly until the required amount of Active Material (AM) is achieved. Periodic boundary conditions and an experimental particle size distribution are applied. The conductive additives and binder (or Carbon Binder Domain -CBD-) inactive phase is added pixel per pixel with the only constraint that it has to be in contact with the solid phase (either active or inactive phase). The second electrode generation approach is our previously reported physical-based Coarse-Grained Molecular Dynamics (CGMD) and Discrete Element Method (DEM) models. The CGMD simulates the electrode slurry and drying steps, while the sequential coupling of CGMD with DEM allows simulating the calendering step. CGMD and DEM models are based on experimental input data such as the AM particle size distribution and explicitly consider the CBD. For further details about our CGMD and DEM models and their validation, the readers are referred to our previous publications [29,30]. The third origin of the cathode mesostructures is micro X-ray tomography of real manufactured elec-

trodes. The electrode consisted in NMC 111 (Umicore), carbon black additive (C-NERGY™ super C65, Imerys) and PVdF (Solef™, Solvay) with a weight composition of 96-2-2. Two different conditions were essayed: uncalendered (ε = 47.8%) and calendered (ε = 26%). The NMC samples obtained by tomography were imported into INNOV for segmentation and the CBD domain added stochastically in a film-like array [28,31]. The micro X-ray tomographic measurements have been conducted at the P05 synchrotron imaging beamline (Desy, Hamburg, Germany) [32]. The data acquisition setup consisted of a KIT CMOS camera combined with a 10 times optic and a 100 μm $CdWO_4$ scintillator yielding an effective pixel size of 0.642 μm. The samples were measured in absorption contrast mode using a photon energy of 25 keV selected by a double multilayer monochromator. For each sample, 2401 projections were measured with equidistant angle steps of 0.15° and an exposure time of 130 ms each. To reduce ring artefacts the center of rotation was shifted by random but tracked values of up to 100 μm. The data was then reconstructed using the filtered back projection algorithm and were further denoised using a 3D non-local means filter [33]. Finally, GeoDict software was used to generate graphite electrode mesostructures. We created a 1000 × 1000 × 1000 voxel domain with a voxel size of 100 nm to make a representative structure. A log-normal particle size distribution was generated by considering the D10, D50 and D90 values to be 8, 11, and 18 μm, respectively. The structure is built in two steps. First spherical particles are homogeneously distributed within the domain, where the total volume fraction that they should occupy is specified. Then the overlaps between the generated objects are removed to approach the specified volume fraction as much as possible. The porosity of the resulting structure without the addition of carbon-binder is 35%. The addition of carbon-binder (using the same algorithm as before) leads to the final porosity of 33%.

All obtained geometries were imported into the INNOV program for the slicing and convert segmentation procedure into binary images, after which a DAT file is created and imported into the LBM simulations [34].

The LBM model developed for this study was based on three dimensional (D3Q19) cubic lattices using both an advection and a collision operator, where Q19 corresponds to fixed velocity vectors per fluid phase or component [35],[36]. A scheme of the lattice structure is shown in Figure 2. The general LBM was initially developed by Shan and Chen and adapted in this work to describe three-dimensional interactions assuming an isothermal system [37]. In the proposed LBM model, motion and fluid-fluid interaction are defined by a set of particle distribution functions based on the Bhatnagar-Gross-Krook (BGK) collision operator where model constants can be used to characterize fluid density and velocity [36]. The left-hand side of equation (1) corresponds to a streaming term, and the right-hand side defines a collision term that together holds the system on Maxwellian equilibrium:[37]

$$f_i(x,\ t) - f_i\left(x + e_i\Delta t,\ t + \Delta t\right) = \frac{\Delta t}{\tau}\left[f_i(x,\ t) - f_i^{eq}(x,\ t)\right] i = 0,\ 1,\ \ldots,\ 18 \tag{1}$$

In the equation above $f_i(x,\ t)$ is the particle distribution function which specifies the number of fluid particles at lattice location x and time t traveling in the i^{th} direction, e_i is a lattice velocity vector that corresponds to allowable directions of the velocity vector, Δt is a discrete time step and τ is the relaxation time. The relaxation parameter represents the rate of particle collisions which is related to the kinematic viscosity (V) of the lattice $V = c_s^2(\tau - \frac{1}{2})$. In this kinematic viscosity expression c^s is the speed of sound of the lattice defined by $c^s = \frac{\frac{\Delta t}{\Delta x}}{\sqrt{3}}$ where $\Delta x = 1$ lattice length unit, *lu*.

As discussed above, the Navier-Stokes macroscopic kinetic theory was applied to describe fluid in the bulk flow at mesoscopic level in the LBM model [26]. The functional form of the equilibrium distribution $f_i^{(eq)} = f(\rho^n v^{n(eq)})$ has the following form for the purpose of recovering the Navier-Stokes equation:

$$f_i^{(eq)}(x,t) = w_i\rho\left[1 + \frac{e_i\rho^{eq}}{c_s^2} + \frac{1}{2}\left(\frac{e_i\rho^{eq}}{c_s^2}\right)^2 - \frac{1}{2}\left(\frac{e_i\rho^{eq}}{c_s^2}\right)^2\right] \tag{2}$$

In the equation above w_i is the weight of each discrete velocity where $w_i = 1/3$ for $i = 0$, $w_i = 1/18$ for $i = 1, \ldots, 6$ and $w_i = 1/36$ for $i = 7, \ldots, 18$. The macroscopic value of density ρ is the density of $f_i(x,\ t)$ and the macroscopic velocity u^{eq} is calculated by $u^{eq} = [\ u_x \quad u_y \quad u_z\ ]$ [26].

The discrete velocities e_i are defined, with their representation given in Figure 2, [38]

$$\begin{bmatrix} e_0, e_1, e_2, e_3, e_4, e_5, e_6, e_7, e_8, e_9, e_{10}, e_{11}, e_{12}, e_{13}, e_{14}, e_{15}, e_{16}, e_{17}, e_{18} \end{bmatrix} = c \begin{bmatrix} 0 & 1 & -1 & 0 & 0 & 0 & 0 & 1 & -1 & -1 & 1 & -1 & 1 & 1 & -1 & 0 & 0 & 0 & 0 \\ 0 & 0 & 0 & 1 & -1 & 0 & 0 & -1 & 1 & -1 & 1 & 0 & 0 & 0 & 0 & 1 & -1 & 1 & -1 \\ 0 & 0 & 0 & 0 & 0 & 1 & -1 & 0 & 0 & 0 & 0 & 1 & 1 & -1 & -1 & -1 & 1 & 1 & -1 \end{bmatrix} \tag{3}$$

The density is obtained by summing the particle densities, $\rho = \sum_i f_i$ and the macroscopic velocity is obtained by summing the particle momentum and dividing by density, $u = \frac{\sum_i f_i e_i}{\rho}$. The external force ($F_{ext}$) is added to the macroscopic velocity as

$$u^{eq} = u + \frac{F_{ext}\tau}{\rho} \tag{4}$$

The two-phase fluid flow is simulated on the lattice by representing each fluid phase with its particle size distribution function as $f_i^{\sigma}(x,t)$, where $\sigma = w, nw$ is the index for each material particle distribution function. Another critical part of the system is the fluid-fluid interaction. In the Shan-Chen model, this interaction is described by interparticle forces ($F_{p,\sigma}$). Equation (5) represents the total fluid-fluid interaction where G_c is the interparticle strength: [26,39,40]

$$F_{p\sigma}(x,t) = -G_c\rho_{\sigma}(x,t)\sum_i w_i\rho_{\sigma}(x + e_i\Delta t, t)e_i \tag{5}$$

Only the nearest-neighbors lattices are active in the calculation of interparticle strength. By choosing the sign and magnitude properly, fluids can be separated to mimic immiscible flow behavior. As described above and shown in equation (6), $\boldsymbol{G_{ads,\sigma}}$ is the interparticle adhesion strength between fluid and solid used to describe the wetting properties of the electrode with the adhesion force

$$F_{ads,\sigma}(x,t) = -G_{ads}\ \rho_{\sigma}(x,t)\sum_i w_i\ e_i\ \cdot s\left(x + e_i\ \Delta t,\ t\right)e_i \tag{6}$$

The negative (positive) values of $\boldsymbol{G_{ads,\sigma}}$ can be used for wetting (nonwetting) fluids, respectively. At the fluid-solid interface, the solid is regarded as a phase with constant density. By carefully selecting the interparticle strength for each liquid-gas and solid phases, experimentally measured contact angle values were used as input for these studies [5]. The calculations of $\boldsymbol{G_{ads,\sigma}}$ were based on

$$\cos\boldsymbol{\theta_w} = \frac{\boldsymbol{G_{ads,nw}} - \boldsymbol{G_{ads,w}}}{\boldsymbol{G_c}\frac{\rho_w - \rho_{nw/w}}{2}} \tag{7}$$

where $\boldsymbol{\rho_w}$ is the density of the wetting fluid and $\boldsymbol{\rho_{nw/w}}$ is the dissolved density of the nonwetting fluid in the wetting fluid [41]. It is important to mention that the fluid-solid-interaction force exists only on the fluid-solid interface and it does not affect the macroscopic fluid equations [42].

The adhesion force created by $\boldsymbol{G_{ads,\sigma}}$ coefficients which are responsible for the wettability of the surface, are added in the model in the

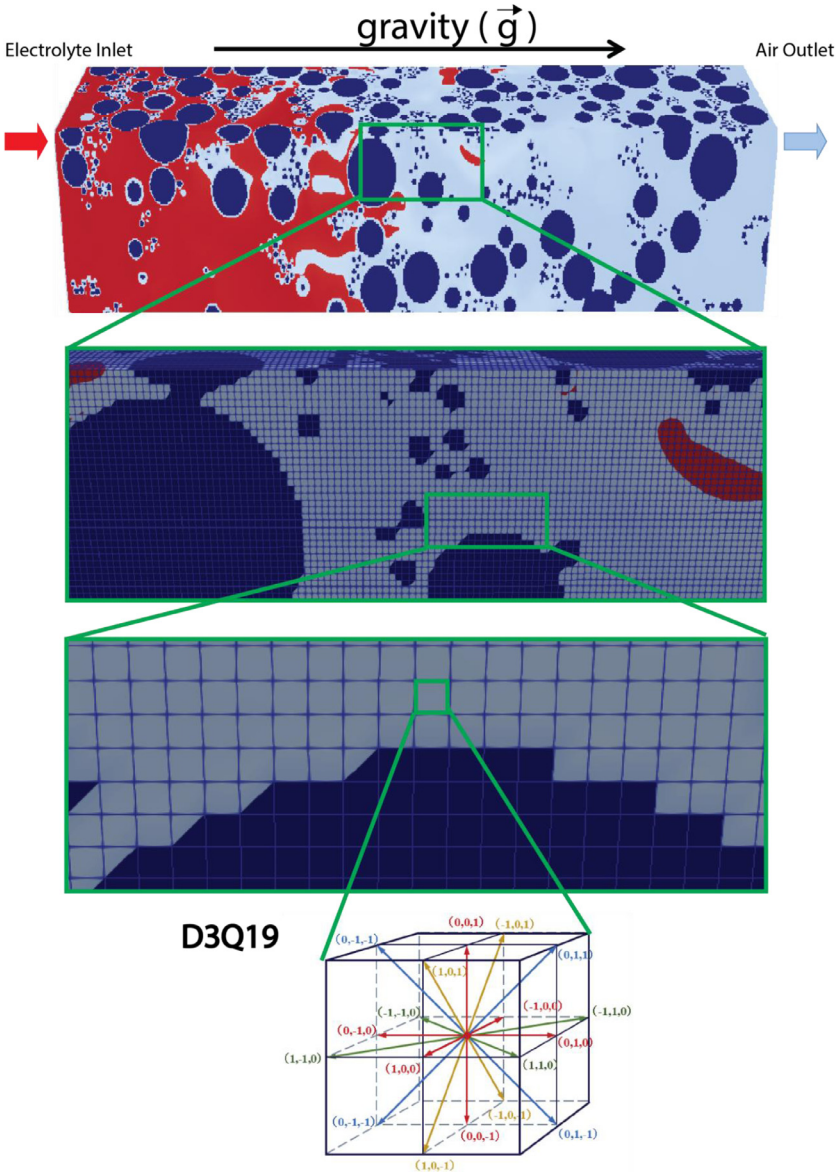

Figure 2. Lattice structure of three-dimensional fifteen velocity (D3Q15) model.

same way like the external forces:

$$\boldsymbol{u}_{\sigma}^{eq} = \boldsymbol{u}' + \frac{\left(\boldsymbol{F}_{ads,\sigma} + \boldsymbol{F}_{p,\sigma} + \boldsymbol{F}_{ext,\sigma}\right)\boldsymbol{\tau}_{\sigma}}{\rho_{\sigma}} \tag{8}$$

The common velocity for the fluids is given by

$$\boldsymbol{u}' = \frac{\sum_{\sigma}\left(\sum_{i} \frac{f_i^{\sigma} e_i}{\tau_{\sigma}}\right)}{\sum_{\sigma} \frac{\rho_{\sigma}}{\tau_{\sigma}}} \tag{9}$$

The lattice pressure (P) at each node is calculated by the D3Q19 Shan-Chen LBM equation: [37,40]

$$\mathbf{P} = \frac{1}{3}\left[\rho_{w} + \rho_{nw}\right] + \frac{1}{3}\left[G_{c}\rho_{w}\rho_{nw}\right] \tag{10}$$

Initially, we assume all the pores within the porous electrodes are filled with air for each LBM simulation. The electrolyte flow enters through the X-axis (thickness) and stops its motion when it reaches the end of the electrode. Periodic boundary conditions along the Y and Z axes were applied. As already mentioned, electrolyte parameters such as the density, contact angle with the solid phase, viscosity and surface tension (equations 1, 6, 7) control the process of liquid injection within the electrode porosity. In this work, we considered an electrolyte composed of a 1M $LiPF_6$ solution in a 1:1 wt mixture of ethylene carbonate (EC) and diethyl carbonate (DEC) where the input parameters were experimentally measured with a BP100 bubble pressure tensiometer (surface tension), volume-changing method (contact angle) and AR 1000 rheometer (viscosity) as reported by one of the authors of the present article [5]. Evidently, selecting the electrolyte and active materials will alter the model's parameters, and exploring this parameter space is worth studying. For instance, using an electrolyte with a higher concentration of salt changes its viscosity, influencing the corresponding model parameters, such as kinematic viscosity (V) and ultimately hindering the electrolyte penetration process [5]. However, this systematic parametric study is beyond the scope of this work. Additionally, we must also note that other known effects that occur due to the electrolyte filling process, such as the swelling of the binder, were not taken into account in our model.

All the input parameters and sizes of simulation boxes are given in Table 1. The LBM simulations were carried out by using the open-source Palabos library version 1.0 [43]. Each simulation took approximately from two to ten days, depending on the simulated system size. The simulations were performed using a laboratory server with 256 Gigabytes of RAM.

Table 1
Simulation inputs and geometry sizes.

Parameter	Lattice value	Physical value
AM 96%-CBD 4% Porosity 25%	100 × 100 × 100 voxels	50 × 50 × 50 μm^3
AM 96%-CBD 4% Porosity 30%	100 × 100 × 100 voxels	50 × 50 × 50 μm^3
AM 96%-CBD 4% Porosity 35%	100 × 100 × 100 voxels	50 × 50 × 50 μm^3
AM 96%-CBD 4% Porosity 40%	100 × 100 × 100 voxels	50 × 50 × 50 μm^3
AM 96%-CBD 4% Porosity 45%	100 × 100 × 100 voxels	50 × 50 × 50 μm^3
AM 96%-CBD 4% Porosity 50%	100 × 100 × 100 voxels	50 × 50 × 50 μm^3
AM 96%-CBD 4% un-calendered tomography	100 × 100 × 75 voxels	100 × 100 × 75 μm^3
AM 96%-CBD 4% calendered tomography	100 × 100 × 75 voxels	100 × 100 × 75 μm^3
AM 96%-CBD 4% un-calendered CGMD	107 × 107 × 603 voxels	107 × 107 × 60.3 μm^3
AM 96%-CBD 4% calendered CGMD+DEM	107 × 107 × 474 voxels	107 × 107 × 474 μm^3
Celgard 2500	100 × 100 × 25 voxels	100 × 100 × 25 μm^3
Graphite 95%-CBD 5%	100 × 100 × 50 voxels	100 × 100 × 50 μm^3
Electrolyte density	10	1300 $\frac{kg}{m^3}$
Gas density	1	1.18 $\frac{kg}{m^3}$ ([63])
Contact angle	0.357/1.643	90° [5]
Surface force (gas-liquid)	0.1	7.28 × 10^{-2} ([5])
t_0	1 lu	1 × 10^{-6} s
Reynolds number	10^{-3}	10^{-3} ([5])
Capillary number	10^{-5}	10^{-5} ([5])

The PoroDict library (within GeoDict) was used to identify the 3D pore network. Pore space segmentation is done using the watershed algorithm [44]. It is known that the surface roughness on the images generally induces over-segmentation in watershed-based methods and many approaches exist to solve it [45-48]. In GeoDict, this is overcame by reconnecting the overly segmented pore-fragments back into a single pore, only if the shared interface percentage between the different pore fragments is larger than a chosen value. This interface threshold value is carefully selected so that the resultant pore sizes are not excessively large with respect to the original structure but are not overly segmented either. Once the pore space is labeled, we calculated the equivalent volume sphere's diameter for each pore and arranged them in a histogram. The histogram is further normalized to account for the non-uniform selection of the number of histogram bins.

In order to import the LBM simulated electrodes into the electrochemical models, the NMC and CBD phases must be separated, as in the LBM workflow both phases are considered as one single solid. For the electrochemical model we used one of the tomography electrodes (see below), and CBD and NMC phases were attained by transforming part of the solid into CBD regions using the same stochastic algorithm mentioned above.

COMSOL Multiphysics environment was used to run electrochemical impedance spectroscopy (EIS) and galvanostatic discharge simulations. The 'Batteries & Fuel Cells' module for the discharge simulations and the 'Batteries & Fuel Cells' and the 'Transport of Diluted species' modules for EIS were implemented for the calculations [34]. The designs of the models and input parameters are identical to our previous reported papers [34,49]. The tests were performed using an Intel® Xeon® E5-4627 Cache @ 3.30 GHz with 264 GB of RAM. The discharge simulations took between 5 and 9 hours and the EIS tests 14 to 20 hours. Paraview, an open-source data analysis and visualization application, was utilized for the visualization of the data [50].

The tortuosity factors were extracted by using GeoDict computational software. The first Fick's law and the MacMullin equation were applied to calculate the tortuosity factors. EIS tortuosity factors were calculated through the graphical method proposed by Landesfeind *et al.* [51-52].

3. Results and discussions

3.1. Stochastically generated electrodes

Five cathode electrodes with different stochastic mesostructures and different porosities were generated to study the mesostructure effect on the electrolyte penetration. As expected, by reducing the porosity, the tortuosity factor ($\tau_{GeoDict}$) increases, as reported in Table 2 [28].

Table 2
Tortuosity for stochastic electrodes with different porosities.

Porosity	25%	30%	35%	40%	45%	50%
$\tau_{Geodict}$	2.20	1.90	1.70	1.53	1.48	1.36

Figure 3A shows the saturation curves for these mesostructures, where the saturation was quantified using the electrolyte volume ratio to the electrode's pore volume. All the cases display a profile with asymptotic growth, where saturation increases very fast at the early stages of impregnation. After a certain point, the gradient decreases and the higher the porosity, the faster the electrolyte penetrates through the porous mesostructure. Furthermore, the slope in the fast growth region tends to be smaller as the porosity decreases. The saturation curves for electrodes with porosities equal to 50% and 45% tend to rise monotonically and reach its maximum saturation before the other ones, indicating that the pore network is well connected and with less clogged areas. On the other hand, the impregnation for the mesostructures with 25% porosity displays slow electrolyte imbibition and reaches saturation at 1.5 × 10^5 lu (Figure 3A). The saturation curves derivatives, which describe the rate of electrolyte filling, are given in Figure 3B. It is clear from the figure that saturation rate tends to decrease with time for all the mesostructures, since the possible paths for fluid flow start to decline. The magnitude of the change in the rate is more significant for the electrodes with higher porosity (40% or higher). When electrode porosity is low, generally, the rate at which the electrolyte penetrates is monotone because the possible paths for fluid flow are limited. Overall, the graph clarifies that the rate of saturation is proportional to the structure's porosity. Figures 3C and 3D represent the outgoing air at different time steps for the electrodes with 50% and 25% porosity, respectively. It further illustrates that the gas escape rate is much faster for the electrode with higher porosity. At 2 × 10^4 lu, all the electrode is already impregnated for the structure with 50 % porosity (Figure 3C), while for the one with 25 % porosity (Figure 3D), more than half of the air remained in the structure at that time step. We can also see some air trapped inside the electrode with 25 % porosity because there are several clogged pores within the geometry, explaining why the electrolyte saturation never reaches 100 %. This result confirms that decreasing the electrodes' porosity increases the wetting time and its unwetted regions.

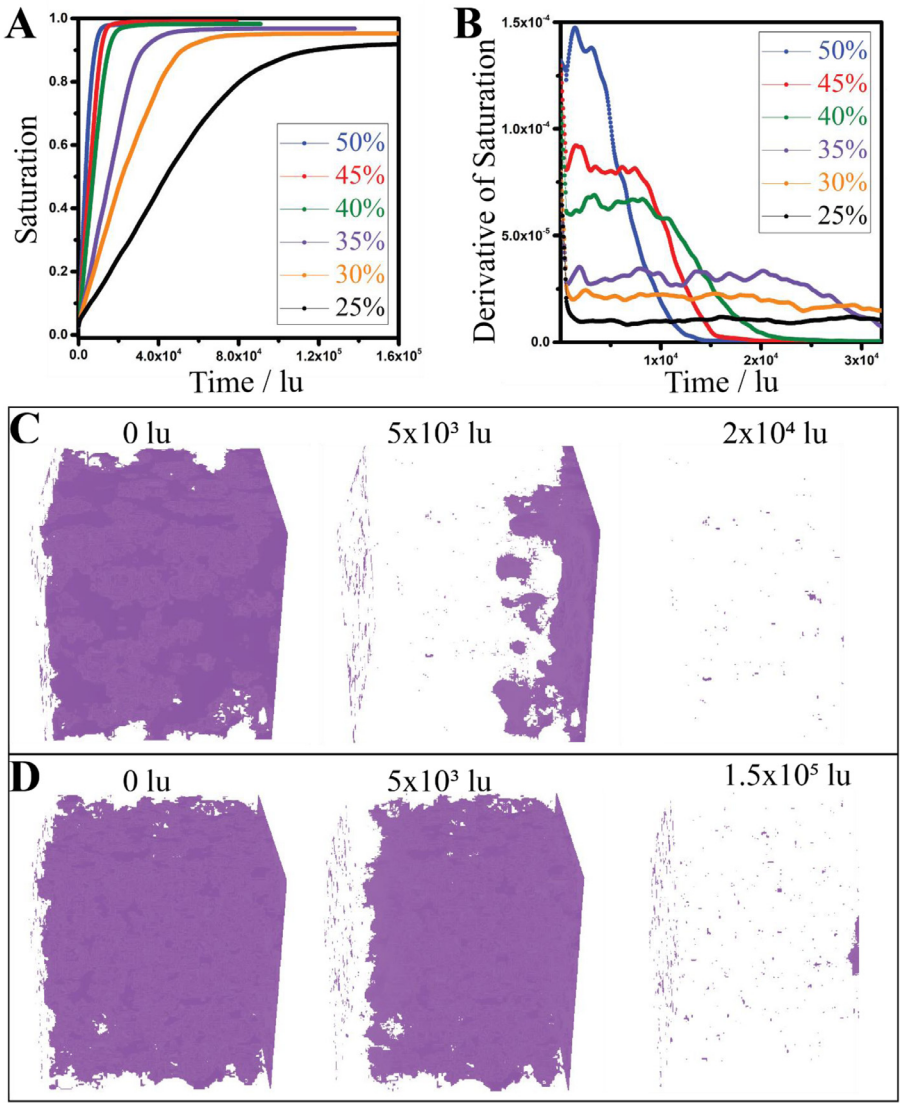

Figure 3. (A) Saturation profile of liquid electrolyte in the cathode with various porosities; (B) the first derivative of the saturation profile of liquid electrolyte in the cathode with various porosities; (C) the air output flow process (in purple) for the electrode with 50% porosity and (D) for the electrode with 25% porosity, at different time steps.

Table 3
Porosity and Tortuosity factor for the uncalendered and calendered NMC111 tomography-derived electrodes.

	Uncalendered tomography	Calendered tomography	Uncalendered CGMD	Calendered CGMD+DEM
Porosity	48%	25%	41.6%	27.2%
$\tau_{Geodict}$	1.53	2.89	1.53	1.92

3.2. Calendering effect

Usually, electrodes are calendered to maximize volumetric power and energy density. The calendering step changes the electrode's porosity, along with its pore size distribution and pore network [46,53]. However, this increased compactness of calendered electrodes might cause incomplete electrolyte wetting. Therefore, in this subsection, the objective is to study the calendering effect over the electrolyte filling on NMC111-based cathodes, obtained through both micro X-ray tomography and CGMD+DEM based simulations.

Table 3 shows the calculated tortuosity factors and porosities for all electrodes used in this subsection. The tortuosity factor increases from 1.53 to 2.89 and porosity decreases from 48 % to 25 % upon calendaring for tomography NMC cathodes. The same trend can be seen for CGMD+DEM-derived electrodes, where tortuosity changed from 1.53 to 1.92 and porosity decreased from 41.6 % to 27.2 %. The negative correlation between porosity and tortuosity factor is expected because electrode compaction leads to pores in general to a decrease of the pores interconnectivity [54].

During the calendering step, the applied force leads to a change in pores size distribution (PSD) within the electrode, which is shown in Figure 4A for the NMC-based cathodes. After the calendering step, the mean pore size was reduced from 15 μm to 5 μm. The same behavior can be seen for CGMD/CGMD + DEM electrodes (Figure 4B), where the mean pore size decreased from 8 μm to 4 μm.

The uncalendered tomography electrode saturation curve (Figure 4C) increases rapidly because of more extended penetration paths and larger pore sizes, as demonstrated in Figure 4A. On the contrary, the wetting process rate for the calendered tomography one is reduced significantly and it never reaches 100% pore saturation, indicating dead pore zones with trapped air. Figure 4D presents the respective saturation curves for uncalendered CGMD and calendered CGMD+DEM electrodes. Equivalently, the saturation is faster for the uncalendered CGMD compared to calendered CGMD+DEM. The difference comes from its higher porosity, lower tortuosity (Table 3), and higher pore size distributions (Figure 4B). As discussed above, higher porosity and PSD cause a better pore network connectivity, which opens a broad path for fluid flow. The saturation reaches it is

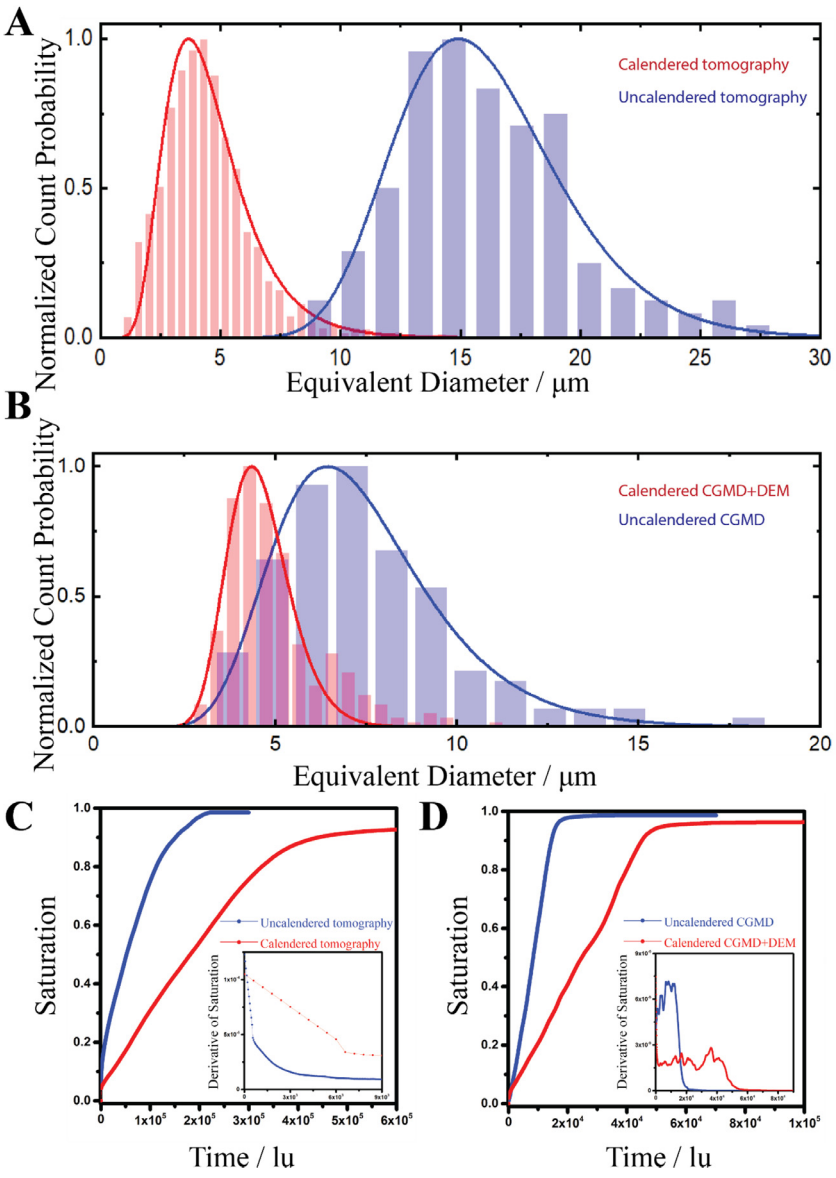

Figure 4. (A) Normalized pore size distribution for uncalendered and calendered tomography NMC 94% - CBD 6%. (B) Normalized pore size distribution for uncalendered and calendered CGMD+DEM. (C) Saturation profile and the first derivative (inset) of the saturation profile of liquid electrolyte for the calendared and uncalendared tomography NMC 94% - CBD 6% electrodes (D) Saturation profile and the first derivative (inset) of liquid electrolyte for the calendered CGMD+DEM and uncalendered CGMD.

maximum at 0.99, and at a rate five times faster, for the uncalendered CGMD, when compared to a maximum of 0.96 for the calendered CGMD + DEM.

The better wettability and faster saturation nature of CGMD/CGMD + DEM structures, when compared to the tomography ones, is found on the shape of the carbon additive and binder domain. CGMD and DEM simulations rely on the assumption that CBD has a spherical shape (due to the coarse-graining assumption in this simulation technique), but it is known that CBD forms a highly anisotropic phase. Due to this fact, electrodes coming from tomography have more geometrically intricated pores than CGMD/CGMD + DEM electrodes. Nevertheless, there is only a three percent difference in saturation between calendered tomography and CGMD + DEM. The global trend for both uncalendered and calendered electrodes between CGMD/CGMD + DEM and tomography cases showed the same pattern and are very closely allied.

The wetting process visualization for the uncalendered and calendered tomography electrodes is shown in Figure 5A. At the beginning of the simulation, there is a higher volume for electrolyte entrance in the uncalendered electrode. As the impregnation proceeds, the bigger and well-connected pores of the uncalendered electrode allow a uniform filling, as it can be seen in the almost plane cross-section electrolyte diffusion direction. The LBM simulations demonstrate the electrolyte occupies large pores first, which means the capillary forces, which result from the pressure difference between electrolyte and air phases, dominate the flow. The electrolyte chooses a preferential flow path within the 3D structure depending on local resistance forces. As a result, the flow is always directed towards a larger pore within the available options. Uncalendered electrode has higher PSD and higher porosity with all the big pores well connected to each other. Consequently, fluid flow is homogenous and fast as represented in Figure 5A. The calendered electrode with its smaller and less connected pores exhibits a non-uniform filling.

This is validated by the air flow in Figure 5B, where air output flow is represented at different time steps for uncalendered and calendared tomography electrodes. It is easy to see the consistent homogenous airflow across all time steps for the uncalendered electrode. Also, at the end of the simulation, there is almost no air trapped within the porous structure. On the contrary, air outflow is heterogenous and slower for the calendered electrode, and there are many air trapped volumes when simulation reaches convergence point. To better understand the nature of the un-filled pores, the geometrical analysis of the calendered electrode pores is performed with our INNOV application [53]. The study

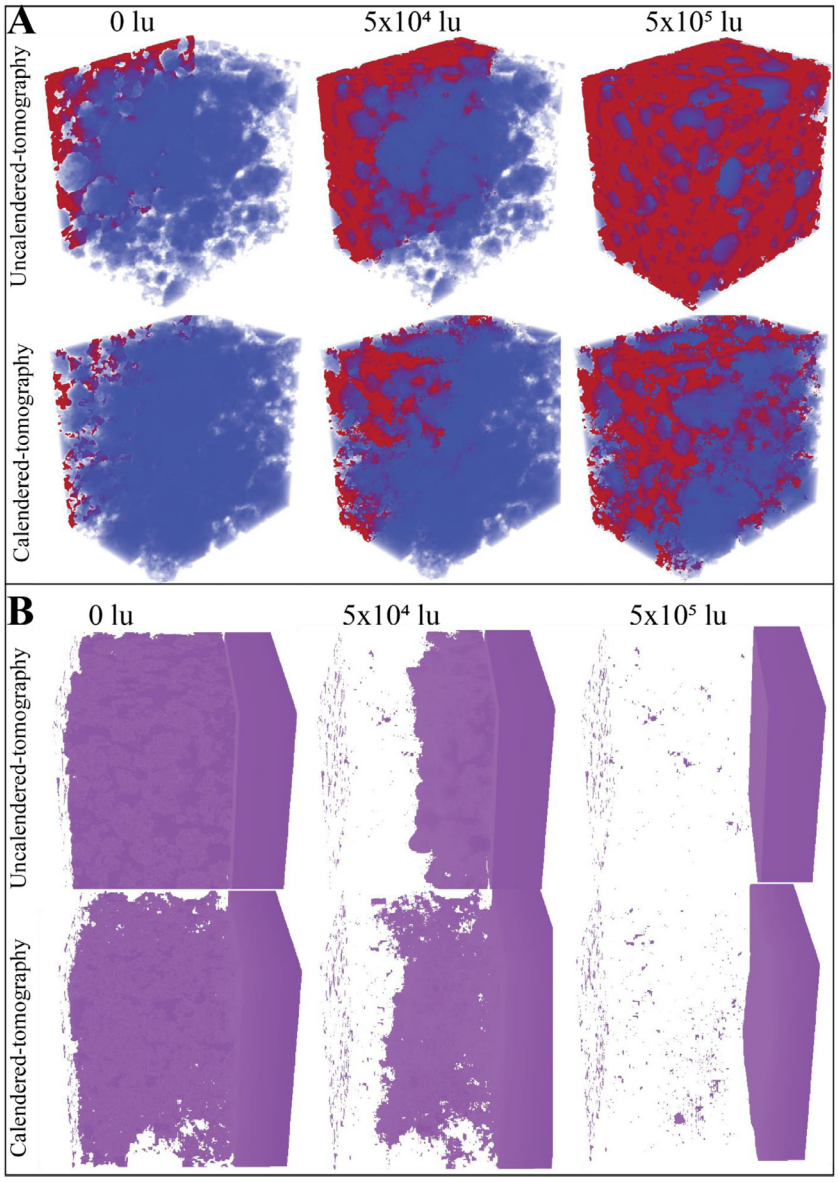

Figure 5. (A) The wetting (red) process visualization for the uncalendered and calendered tomography electrodes (NMC 94% - CBD 6%) (blue) at different time steps; (B) the gaseous air (purple) in uncalendered and calendered tomography electrodes (NMC 94% - CBD 6%) electrode at different time steps.

reveals the volume fraction of geometrically blocked pores equal to 5% of total volume and it is mostly responsible for creating unwetted zones.

To better understand the impact of the PSD on the electrolyte impregnation process, the pores were split into three groups: big, medium, and small. Each group corresponds to one-third of the total pore volume. Figures 6A and B present the saturation curves for each pore group for the tomography uncalendered and calendered electrodes. For the former, big and medium pores show almost the same slope. On the other side, the saturation rate is slower for the small pores, and it does not reach its maximum, indicating that all the geometrically isolated unwetted pores come from this group. In the case of the calendered tomography electrode, the saturation rate for all the groups decreased, compared to the uncalendered electrode, and none of them reached its maximum.

Like tomography-derived electrodes, all big pores in the CGMD/CGMD + DEM-based ones (Figures 6C and D) reached 100% saturation and the small pores have the lowest maximum saturation for both electrodes. We note also in Figure 6C, contrary to the Figures 6A, 6B and 6D, that the medium-pores group shows higher saturation rate compared to the big-pores one. We know that the electrolyte penetration rate depends on the porosity, tortuosity factor and pore size distribution of the electrode. The data shown in Table 3 shows that the uncalendered tomography (Figure 6A) and CGMD (Figure 6C) electrodes' porosity and tortuosity factors are almost similar. However, we hypothesize that this phenomenon's origin is related to the electrode's discontinuous pore network organization [55]. Along the thickness of the CGMD electrode, the three groups' population is not homogeneous, which leads to different groups dominating fluid flow across different portions along the thickness. We think that the fluid inlet is mainly populated with big pores, which leads to an increment of saturation at the early stage. When electrolyte reaches some depth in the electrode where pores with big size might be absent, flow is dominated by other groups. Even though average electrode properties are the same for both uncalendered tomography and uncalendered CGMD, their respective pore networks are not the same, which may explain the counter-intuitive behavior of Figure 6C [56].

As discussed above, the calendering step decreases the electrode porosity and pore sizes, potentially creating more geometrically isolated pores. The idea that compressing the electrode creates clogged pores with a small size proved itself once more. These results suggest that calendering the electrode to gain power density would be negatively correlated with the electrode's wettability which is consistent with the

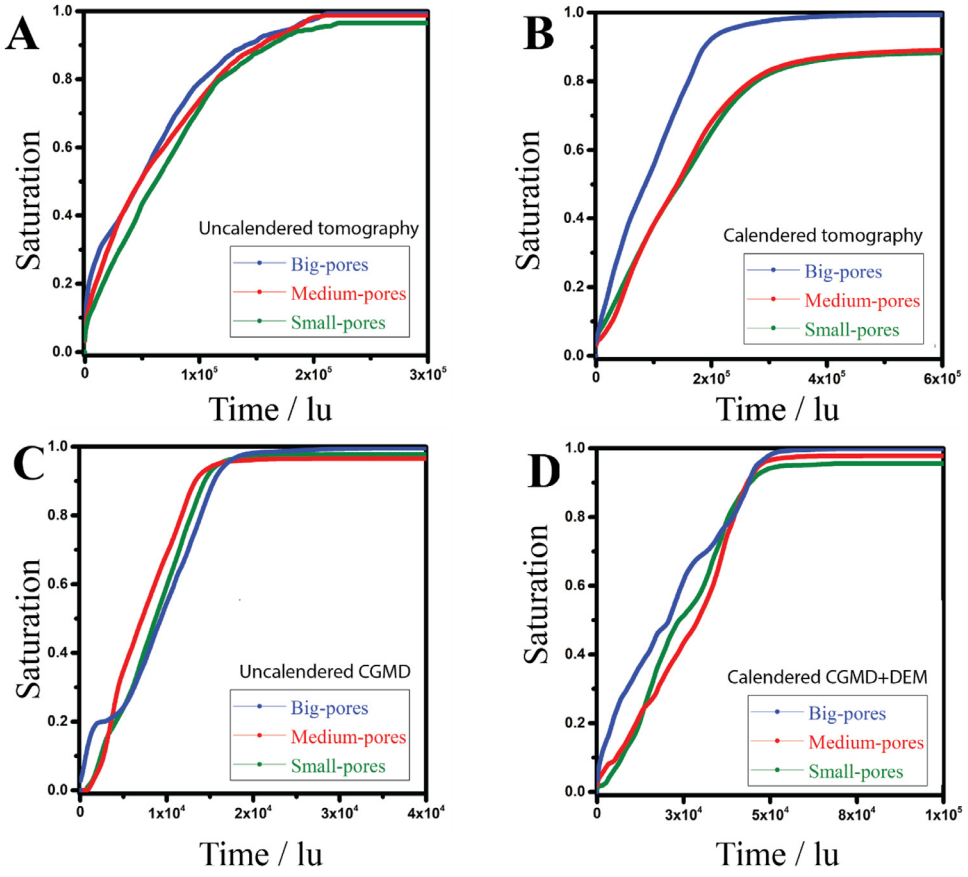

Figure 6. Saturation profiles of liquid electrolyte for the three pore groups (big, medium, and small) within (A) the uncalendered tomography electrode (NMC 94% - CBD 6%), (B) the the calendered tomography electrode (NMC 94% - CBD 6%), (C) the uncalendered CGMD electrode and (D) the calendered CGMD+DEM electrode.

Table 4
Porosity and tortuosity factor for graphite electrode and Celgard2500 separator.

	Graphite	Celgard2500	Uncalendered tomography
Porosity	31.5%	55%	48%
$\tau_{Geodict}$	1.63	1.49	1.53

experimental results [10]. While the results are also in good agreement with intuition, our model allows providing quantitative results which have never been reported before, such as the correlation between saturation rate, processing conditions and mesostructure. We believe that achieving optimally performing electrodes requires solving the compromise between the calendering process and the electrolyte filling step. In short, better electronic conduction is achieved by calendering, but it could result in clogged and poorly connected pores that hinder the electrolyte penetration. Therefore, we recognize that keeping a well connected pore-network upon calendering is vital.

3.3. Electrolyte infiltration direction in full cells

Conventionally, during LIB manufacturing process, the different parts of the cell are assembled in a sandwich format before filling with the electrolyte [4,57]. Therefore, NMC111, Celgard 2500, and Graphite electrodes were put together to construct the full LIB format and run LBM simulations [53]. The porosities and tortuosity factors for the separator and the negative electrode are given in Table 4.

The saturation curves corresponding to the electrolyte inlet from two different sides of the full cell, are presented in Figure 7A. The saturation curves show several different plateaus and dynamic steps in both cases. When the electrolyte impregnation inlet is from the NMC the cell behaves precisely like the NMC electrode (Figure 4C). At around time step 4.5×10^4 lu the saturation speed increases when the electrolyte reaches the separator (Figure 7B). In it, the fluid goes relatively faster because the separator has a higher porosity and a very well interconnected porous structure, as seen in the Supporting Information (Figure S2). At about 5.2×10^4 lu, the curve trend changes again as the fluid reaches the graphite electrode. The speed decreases drastically as the porosity of the negative electrode is smaller compared to the separator and the positive electrode, reaching the convergence at around 1.2×10^5 lu (Figure 7B). The graphite and separator structures are 100% wetted and all the unwetted zones are coming from NMC structure due to isolated pores as discussed above. The same three-step behavior can be observed for the cell setup where the electrolyte inlet is on the negative electrode. The origin of the three steps again comes from the microstructure and PSD of the three different components. The electrolyte impregnation speed is slower than in the previous case because the initial available space for the electrolyte entrance is smaller in the graphite electrode. The path of the electrolyte at different time steps is shown for both cells in Figures 7C and 7D. Overall, the full cell studies showed the importance of the order of the components within the cell. Also, the initial electrolyte entrance location plays a crucial role in the LIB cell overall wetting time. It is worthy to note that electrolyte won't penetrate through the electrode stacks from anode to cathode or vice versa unless porous current collectors are used. Nevertheless, this result shows that the starting location of electrolyte injection can impact the overall electrolyte wetting process. This effect is under further investigation and will be reported in our future publications.

3.4. In silico electrochemical performance evaluations

In this section we study the electrolyte impregnation effect on the electrochemical performance of the electrode by means of continuum

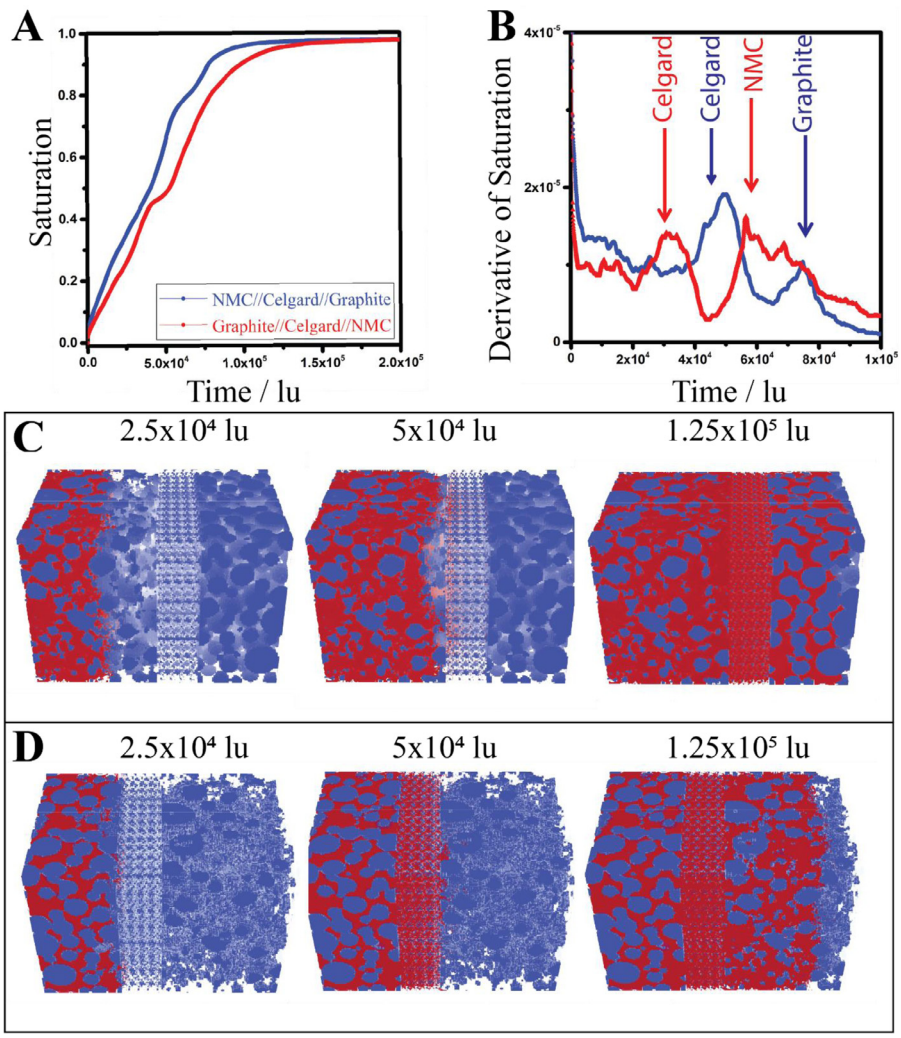

Figure 7. (A) Saturation curve for the NMC//Celgard//Graphite and Graphite//Celgard//NMC cells;; (B) the first derivative of the saturation profile of liquid electrolyte, the wetting (red) process' visualization for (C) NMC//Celgard//Graphite (blue) and (D) Graphite//Celgard//NMC (blue) at different time steps.

simulations. The electrochemical model is 4D-resolved (three spatial dimensions and time), and it accounts for the explicit location of AM and CBD in the electrode mesostructure. It resolves the intercalation electrochemistry at the NMC/electrolyte interface (for the case of the discharge simulation), the electrical double layer formation within CBD and at the CBD/electrolyte interfaces (for the case of EIS simulation), the lithium transport in the NMC (for the case of the discharge simulation), ionic transport in the electrolyte and in the CBD, electronic transport in both NMC and CBD. Related mathematical details and used parameters are described in our previous publications [49,58]. The following study was carried out for the case of the tomography-derived calendered NMC electrode.

Our 4D-resolved EIS model applied to an *in silico* symmetric cell setup already proved valuable to capture ionic and electronic resistance within the electrode [58]. We use it here to capture the effect of unwetted zones on the change in ionic resistance within the electrode. The symmetric cell consists of two identical electrodes, separated by a 12 μm thick Celgard separator based on the SEM images from the open-source data of Lagadec *et al.* [59] Two 5 μm thick aluminum current collectors were added at each electrode borne, and simulations were carried out by assuming a blocking electrolyte [60]. Figure 8A shows the Nyquist plots for the two cases: one assuming that all the pores are filled with electrolyte and another one corresponding to the wetted electrode according to LBM results. The corresponding response can be analyzed by dividing it into three regions. The high-frequency region (> 10^5 Hz) is associated with the separator's resistance and the electrode's electronic resistance [52,58]. As the electrode architecture was not changed during the LBM simulation, both curves overlap in the high-frequency region plot. On the other side, the low-frequency (< 1Hz) region for both cases shows an ideal 90° behavior as the electrode/electrolyte interface is ideally polarizable, with constant electrical double layer capacitance [61]. Usually, the slopping mid-frequency (1-10^5 Hz) region represents electrolyte ionic resistance within the porous electrode [58],[52]. It can be seen that the length of the mid-frequency slope increases for the electrode with unwetted zones. This phenomenon's origin is that the ions have to take a longer path for the electrode with unwetted zones, as illustrated schematically in Figure 9 . Moreover, the length of the slope directly links to the EIS tortuosity factor (τ_{EIS}) [52]. Calculated tortuosity factors from the EIS (τ_{EIS}) are shown in Table 5.

The discharge curves for both electrodes at C/20 are reported in Figure 8B. The post-LBM electrode displays a lower specific capacity than the one entirely filled with electrolyte. This behavior is expected since it has been shown earlier that the unwetted zones will hinder the transport of ions and reduce the active surface area where Li^+ can intercalate (see Figure 9). The inset in Figure 8B represents the relative amount of intercalated Li in the AM at the surface in contact with unwetted areas to further prove the latter. In the post-LBM electrode case, this surface will be inactive and the only way Li can access these regions will be by diffusion through the AM. In the other case, Li^+ will intercalate at this surface, hence a higher lithiation state for the 100

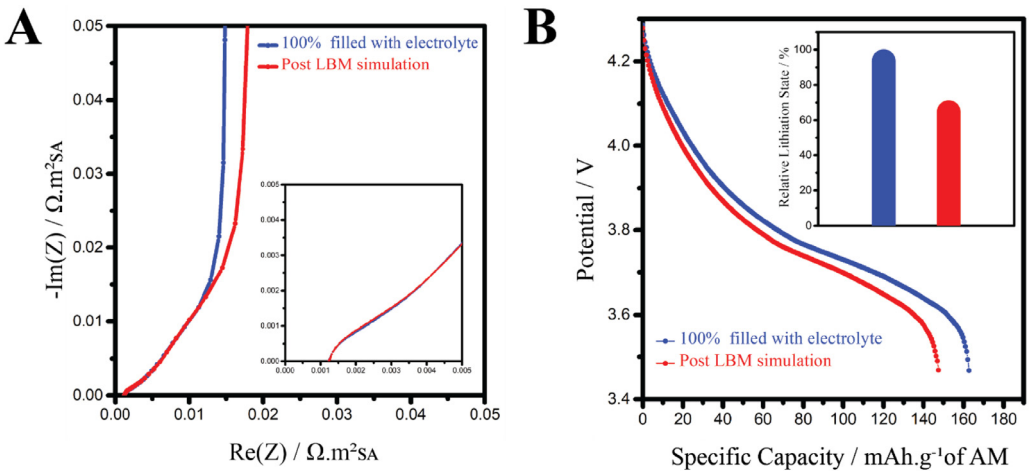

Figure 8. Simulated EIS and discharge models for the calendered tomography NMC 96% - CBD 4% electrode filled with 100% electrolyte and post LBM electrolyte infiltration simulation (A) Nyquist plots in the symmetric cell configuration, (B) Discharge curves at C/20 for the LBM output and the 100% filled electrode (the inset shows the average lithiation state of the AM surface in contact with the unfilled void at the end of discharge, -red- in comparison with the fully infiltrated electrode case -blue-).

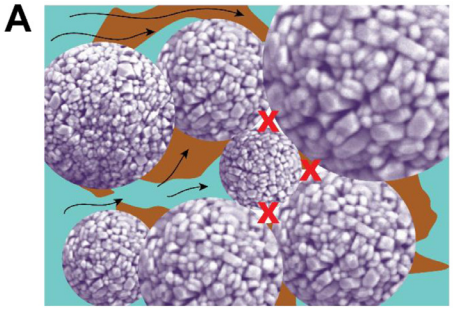

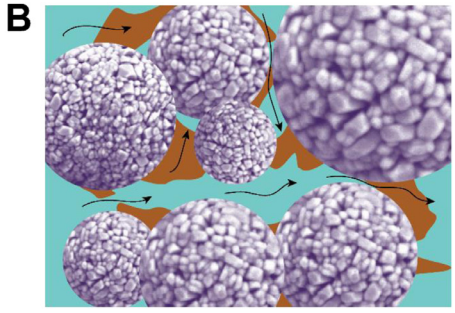

Figure 9. Schematics of ionic paths during the simulation of the electrochemical response (EIS or discharge) of the calendered tomography NMC 96% - CBD 4% electrodes for the case where the electrolyte does not fully fill the pores as calculated by the LBM for (A). The case where electrolyte is assumed to fill all the pores of the electrode is shown in (B). Blue colour represents the electrolyte while brown colours represents the CBD.

Table 5
Ionic resistances (R_{ion}) of the electrolyte within the porous electrode and associated tortuosity factors (τ_{EIS}) calculated according to the Transmission Line Model proposed by Landesfeind et al. [52]

	R_{ion} (Ω m^2) [a]	τ_{EIS} [b]
100% filled with electrolyte	0.014	2.02
Post LBM simulations	0.0162	2.36

[a] Obtained from the graphical interpolation of the high-to-mid frequency region on the EI spectra. [b] EIS-derived tortuosity obtained through the graphical method according to Landesfeind *et al.*

% filled with electrolyte electrode compared to the post-LBM electrode case (100% and 64.7%, respectively). These heterogeneities in Li intercalation arising from the electrode filling will cause the electrode to have steeper Li concentration gradients, hence a higher polarization and a loss in capacity [49]. The combination of the two electrochemical models allowed us to characterize the wetting degree's impact thoroughly. The results demonstrated that the dry electrode mesostructure is not the only impactful parameter, but its degree of wettability is also crucial in its overall electrochemical performance.

4. Conclusion

A novel three-dimensional LBM was developed to simulate electrolyte filling in different LIB cathode mesostructures and full cells. The LBM simulates unsteady fluid flow and two-phase (electrolyte and air) interface evolution during the electrolyte passage through the mesostructures. This model allowed us to visualize the electrolyte penetration and to characterize in depth the wettability process. The electrodes from three different sources (stochastic, tomography, CGMD/DEM) were used in this simulation study.

The results indicate that porous electrodes' wettability is strongly linked to their porosity, pore size distribution, tortuosity factor and pore network organization. Also, the effect of calendering on the wettability is found to be very significant. The studies further revealed that the geometrically isolated pores play a major role in electrodes' poor wettability. The full cell setup investigations demonstrated that the degree of electrolyte penetration in each electrode also strongly depends on the initial electrolyte droplets' location. An extension of this study to other setup configurations is currently carried out by our group, which may give accurate suggestions as to where to set the initial electrolyte inlet for optimal filling. Also, electrochemical simulations were performed to assess the effect of wettability on the positive electrode's overall performance. These simulations show that poor wettability leads to increased ionic resistance and inhomogeneous lithium intercalation, resulting in a lower capacity vs. the case where the electrolyte is supposed to fully fill the electrode pores, as typically assumed in many performance mathematical models in the literature. The simulation tool reported in this work will be integrated in the overall computational workflow of our ARTISTIC project simulating all the steps of the LIB electrode manufacturing process, including the electrode slurry, the coating, the drying, the calendering, the electrolyte infiltration and the resulting electrochemical performance [62].

Nomenclature

Mathematical notations and list of symbols

$f_i(\boldsymbol{x}, t)$	Distribution function of the fluid component
$\boldsymbol{x}$	Lattice location
t	Traveling time
Δt	Discrete time step
i	ith direction
$\boldsymbol{e}_i$	Lattice velocity vector
τ	Relaxation time
$\boldsymbol{u}^{eq}$	Macroscopic velocity
$\boldsymbol{e}_i$	Discrete velocities
$\boldsymbol{F}_{ext}$	External force
ρ	Fluid density
ρ_w	Density of the wetting fluid
$\boldsymbol{w}_i$	Weight of each discrete velocity i
c^s	Speed of sound
V	Kinematic viscosity
$\boldsymbol{v}^{n(eq)}$	Equilibrium velocity
$\boldsymbol{F}^n$	Total interaction force for fluid n
$\boldsymbol{G}_c$	Interparticle strength
$\boldsymbol{G}_{ads,\sigma}$	Fluid-solid interparticle strength
$\boldsymbol{P}$	Lattice pressure

Declaration of Competing Interest

The authors declare that they have no known competing financial interests or personal relationships that could have appeared to influence the work reported in this paper.

Acknowledgment

The authors acknowledge the European Union's Horizon 2020 research and innovation programme for the funding support through the European Research Council (grant agreement 772873, "ARTISTIC" project). A.A.F. also acknowledges the Institut Universitaire de France for the support Furthermore, we thank Fabian Wilde and Tobias Arlt for the support at the P05 synchrotron beamline at DESY.

Supplementary materials

Supplementary material associated with this article can be found, in the online version, at doi:10.1016/j.ensm.2021.02.029.

References

[1] A.A. Franco, A. Rucci, D. Brandell, C. Frayret, M. Gaberscek, P. Jankowski, P. Johansson, Boosting Rechargeable Batteries R&D by Multiscale Modeling: Myth or Reality? Chem. Rev. 119 (2019) 4569–4627, doi:10.1021/acs.chemrev.8b00239.

[2] R. Borah, F.R. Hughson, J. Johnston, T. Nann, On battery materials and methods, Mater. Today Adv 6 (2020) 100046, doi:10.1016/j.mtadv.2019.100046.

[3] T. Knoche, F. Surek, G. Reinhart, A Process Model for the Electrolyte Filling of Lithium-ion Batteries, Procedia CIRP 41 (2016) 405–410, doi:10.1016/j.procir.2015.12.044.

[4] D.L. Wood, J. Li, S.J. An, Formation Challenges of Lithium-Ion Battery Manufacturing, Joule 3 (2019) 2884–2888, doi:10.1016/j.joule.2019.11.002.

[5] A. Davoodabadi, J. Li, Y. Liang, D.L. Wood, T.J. Singler, C. Jin, Analysis of electrolyte imbibition through lithium-ion battery electrodes, J. Power Sources. 424 (2019) 193–203, doi:10.1016/j.jpowsour.2019.03.115.

[6] D.L. Wood, J. Li, C. Daniel, Prospects for reducing the processing cost of lithium ion batteries, J. Power Sources. 275 (2015) 234–242, doi:10.1016/j.jpowsour.2014.11.019.

[7] K. Pfeifer, S. Arnold, J. Becherer, C. Das, J. Maibach, H. Ehrenberg, S. Dsoke, Can Metallic Sodium Electrodes Affect the Electrochemistry of Sodium-Ion Batteries? Reactivity Issues and Perspectives, ChemSusChem 12 (2019) 3312–3319, doi:10.1002/cssc.201901056.

[8] K. Pfeifer, M.F. Greenstein, D. Aurbach, X. Luo, H. Ehrenberg, S. Dsoke, Interaction between Electrolytes and Sb2O3-Based Electrodes in Sodium Batteries: Uncovering the Detrimental Effects of Diglyme, ChemElectroChem 7 (2020) 3487–3495, doi:10.1002/celc.202000894.

[9] D.H. Jeon, Wettability in electrodes and its impact on the performance of lithium-ion batteries, Energy Storage Mater 18 (2019) 139–147, doi:10.1016/j.ensm.2019.01.002.

[10] A. Davoodabadi, J. Li, H. Zhou, D.L. Wood, T.J. Singler, C. Jin, Effect of calendering and temperature on electrolyte wetting in lithium-ion battery electrodes, J. Energy Storage. 26 (2019) 101034, doi:10.1016/j.est.2019.101034.

[11] S.G. Lee, D.H. Jeon, B.M. Kim, J.H. Kang, C.-J. Kim, Lattice Boltzmann Simulation for Electrolyte Transport in Porous Electrode of Lithium Ion Batteries, J. Electrochem. Soc. 160 (2013) H258-H265, doi:10.1149/2.017306jes.

[12] A. Davoodabadi, C. Jin, D.L. Wood, T.J. Singler, J. Li, On electrolyte wetting through lithium-ion battery separators, Extrem. Mech. Lett. (2020) 40, doi:10.1016/j.eml.2020.100960.

[13] F.J. Günter, C. Burgstaller, F. Konwitschny, G. Reinhart, Influence of the Electrolyte Quantity on Lithium-Ion Cells, 166 (2019). 10.1149/2.0121910jes.

[14] W.J. Weydanz, H. Reisenweber, A. Gottschalk, M. Schulz, T. Knoche, G. Reinhart, M. Masuch, J. Franke, R. Gilles, Visualization of electrolyte filling process and influence of vacuum during filling for hard case prismatic lithium ion cells by neutron imaging to optimize the production process, J. Power Sources. 380 (2018) 126–134, doi:10.1016/j.jpowsour.2018.01.081.

[15] A. Schilling, S. Wiemers-Meyer, V. Winkler, S. Nowak, B. Hoppe, H.H. Heimes, K. Dröder, M. Winter, Influence of Separator Material on Infiltration Rate and Wetting Behavior of Lithium-Ion Batteries, Energy Technol 8 (2020) 1900078, doi:10.1002/ente.201900078.

[16] S. Beyer, O. Kobsch, D. Pospiech, F. Simon, C. Peter, K. Nikolowski, M. Wolter, B. Voit, Influence of surface characteristics on the penetration rate of electrolytes into model cells for lithium ion batteries, J. Adhes. Sci. Technol. 34 (2020) 849–866, doi:10.1080/01694243.2019.1686831.

[17] C. Peter, K. Nikolowski, S. Reuber, M. Wolter, A. Michaelis, Chronoamperometry as an electrochemical in situ approach to investigate the electrolyte wetting process of lithium-ion cells, J. Appl. Electrochem. 50 (2020) 295–309, doi:10.1007/s10800-019-01383-2.

[18] T. Knoche, V. Zinth, M. Schulz, J. Schnell, R. Gilles, G. Reinhart, In situ visualization of the electrolyte solvent filling process by neutron radiography, J. Power Sources. 331 (2016) 267–276, doi:10.1016/j.jpowsour.2016.09.037.

[19] A. Schilling, P. Gümbel, M. Möller, F. Kalkan, F. Dietrich, K. Dröder, X-ray Based Visualization of the Electrolyte Filling Process of Lithium Ion Batteries, J. Electrochem. Soc. 166 (2019) A5163-A5167, doi:10.1149/2.0251903jes.

[20] A. Davoodabadi, J. Li, Y. Liang, R. Wang, H. Zhou, D.L. Wood, T.J. Singler, C. Jin, Characterization of Surface Free Energy of Composite Electrodes for Lithium-Ion Batteries, J. Electrochem. Soc. 165 (2018) A2493-A2501, doi:10.1149/2.0341811jes.

[21] H78177.pdf, (n.d.).

[22] M. Quadrio, C. Pipolo, S. Corti, R. Lenzi, F. Messina, C. Pesci, G. Felisati, Review of computational fluid dynamics in the assessment of nasal air flow and analysis of its limitations, Eur. Arch. Oto-Rhino-Laryngology. 271 (2014) 2349–2354 10.1007/s00405-013-2742-3.

[23] S. Takenaka, K. Suga, T. Kinjo, S. Hyodo, Flow Simulations in a Sub-Micro Porous Medium by the Lattice {B}oltzmann and the Molecular Dynamics Methods, in: ASME Conf. Proc, 2009, pp. 927–936, doi:10.1115/ICNMM2009-82062. 2009.

[24] E.. Viggen, The lattice Boltzmann method: Fundamentals and acoustics, 2014. ISBN 978-82-326-0037-3.

[25] L. Chen, Q. Kang, Y. Mu, Y.L. He, W.Q. Tao, A critical review of the pseudopotential multiphase lattice Boltzmann model: Methods and applications, Int. J. Heat Mass Transf. 76 (2014) 210–236, doi:10.1016/j.ijheatmasstransfer.2014.04.032.

[26] C. Pan, M. Hilpert, C.T. Miller, Lattice-Boltzmann simulation of two-phase flow in porous media, Water Resour. Res. 40 (2004) 1–14, doi:10.1029/2003WR002120.

[27] S.G. Lee, D.H. Jeon, Effect of electrode compression on the wettability of lithium-ion batteries, J. Power Sources. 265 (2014) 363–369, doi:10.1016/j.jpowsour.2014.04.127.

[28] M. Duquesnoy, T. Lombardo, M. Chouchane, E.N. Primo, A.A. Franco, Data-driven assessment of electrode calendering process by combining experimental results, in silico mesostructures generation and machine learning, J. Power Sources. 480 (2020) 229103, doi:10.1016/j.jpowsour.2020.229103.

[29] T. Lombardo, J.-B. Hoock, E. N Primo, A. C Ngandjong, A. Rucci, M. Duquesnoy, G. Shukla, J. Vazquez-Arenas, A. A. Franco, Accelerated Optimization Methods for Force-Field Parametrization in Battery Elelctrode Manufacturing Modeling, Batteries & Supercaps 3 (8) (2020) 721–730 https://doi.org/10.1002/batt.202000049.

[30] A.C. Ngandjong, T. Lombardo, E.N. Primo, M. Chouchane, A. Shodiev, O. Arcelus, A.A. Franco, Investigating electrode calendering and its impact on electrochemical performance by means of a new discrete element method model: Towards a digital twin of Li-Ion battery manufacturing, J. Power Sources. 485 (2021) 229320, doi:10.1016/j.jpowsour.2020.229320.

[31] M. Duquesnoy, T. Lombardo, M. Chouchane, E.N. Primo, A. Alejandro, Accelerating Battery Manufacturing Optimization by Combining Experiments, in: Silico Electrodes Generation and Machine Learning, ChemRxiv. Prepr, 2020, pp. 1–33, doi:10.26434/chemrxiv.12473501.v.

[32] F. Wilde, M. Ogurreck, I. Greving, J.U. Hammel, F. Beckmann, A. Hipp, L. Lottermoser, I. Khokhriakov, P. Lytaev, T. Dose, H. Burmester, M. Müller, A. Schreyer, Micro-CT at the imaging beamline P05 at PETRA III, AIP Conf. Proc. 1741 (2016) 10-14. 10.1063/1.4952858.

[33] P. Coupe, P. Yger, S. Prima, P. Hellier, C. Kervrann, C. Barillot, An optimized blockwise nonlocal means denoising filter for 3-D magnetic resonance images, IEEE Trans. Med. Imaging. 27 (2008) 425–441, doi:10.1109/TMI.2007.906087.

[34] M. Chouchane, A. Rucci, A.A. Franco, A Versatile and Efficient Voxelization-Based Meshing Algorithm of Multiple Phases, ACS Omega 4 (2019) 11141–11144, doi:10.1021/acsomega.9b01279.

[35] Y.H. Qian, D. D'Humières, P. Lallemand, Lattice bgk models for navier-stokes equation, Epl 17 (1992) 479–484, doi:10.1209/0295-5075/17/6/001.

[36] D.A. Perumal, A.K. Dass, A Review on the development of lattice Boltzmann computation of macro fluid flows and heat transfer, Alexandria Eng. J. 54 (2015) 955–971, doi:10.1016/j.aej.2015.07.015.

[37] X. Shan, H. Chen, Lattice Boltzmann model for simulating flows with multi phases and componentsShan, X., & Chen, H. (1993). Lattice Boltzmann model for simulating flows with multi phases and components. Physical Review E, 47(3), 1815-1819. 10.1103/PhysRevE., Phys. Rev. E. 47 (1993) 1815-1819. 10.1103/PhysRevE.47.1815.

[38] Y. Cha, S.S. Park, K. Kim, M. Byeon, C.A. Stow, Water Resources Research (2014) 5375–5377, doi:10.1002/2013WR014979.Reply.

[39] J. Zhu, J. Ma, Extending a Gray Lattice Boltzmann Model for Simulating Fluid Flow in Multi-Scale Porous Media, Sci. Rep. 8 (2018) 1–19, doi:10.1038/s41598-018-24151-2.

[40] X. Shan, G. Doolen, Multicomponent lattice-Boltzmann model with interparticle interaction, J. Stat. Phys. 81 (1995) 379–393, doi:10.1007/BF02179985.

[41] H. Huang, D.T. Thorne, M.G. Schaap, M.C. Sukop, Proposed approximation for contact angles in Shan-and-Chen-type multicomponent multiphase lattice Boltzmann models, Phys. Rev. E - Stat. Nonlinear, Soft Matter Phys. 76 (2007) 1–6, doi:10.1103/PhysRevE.76.066701.

[42] N.S. Martys, H. Chen, Simulation of multicomponent fluids in complex three-dimensional geometries by the lattice Boltzmann method, Phys. Rev. E - Stat. Physics, Plasmas, Fluids, Relat. Interdiscip. Top. 53 (1996) 743–750, doi:10.1103/PhysRevE.53.743.

[43] J. Latt, O. Malaspinas, D. Kontaxakis, A. Parmigiani, D. Lagrava, F. Brogi, M. Ben Belgacem, Y. Thorimbert, S. Leclaire, S. Li, F. Marson, J. Lemus, C. Kotsalos, R. Conradin, C. Coreixas, R. Petkantchin, F. Raynaud, J. Beny, B. Chopard, Palabos: Parallel Lattice Boltzmann Solver, Comput. Math. with Appl., 2020, doi:10.1016/j.camwa.2020.03.022.

[44] S. Beucher, C. Lantuejoul, Use of Watersheds in Contour Detection, Int. Work. Image Process. Real-Time Edge Motion Detect. (1979) 12-21. http://www.citeulike.org/group/7252/article/4083187.

[45] M. Waseem Khan, A Survey, Image Segmentation Techniques, Int. J. Futur. Comput. Commun. (2014) 89–93, doi:10.7763/ijfcc.2014.v3.274.

[46] F.L.E. Usseglio-Viretta, D.P. Finegan, A. Colclasure, T.M.M. Heenan, D. Abraham, P. Shearing, K. Smith, Quantitative Relationships Between Pore Tortuosity, Pore Topology, and Solid Particle Morphology Using a Novel Discrete Particle Size Algorithm, J. Electrochem. Soc. 167 (2020) 100513, doi:10.1149/1945-7111/ab913b.

[47] F.L.E. Usseglio-viretta, K. Smith, Quantitative Microstructure Characterization of a NMC Electrode Transportation and Hydrogen Systems Center, National Renewable Energy Laboratory, Golden, Colorado 80401-3305, USA Performance of lithium-ion batteries (LIBs) is strongly influenced by, 77 (2017) 1095-1118.

[48] L. Holzer, B. Muench, M. Wegmann, P. Gasser, R.J. Flatt, FIB-nanotomography of particulate systems - Part I: Particle shape and topology of interfaces, J. Am. Ceram. Soc. 89 (2006) 2577–2585, doi:10.1111/j.1551-2916.2006.00974.x.

[49] M. Chouchane, A. Rucci, T. Lombardo, A.C. Ngandjong, A.A. Franco, Lithium ion battery electrodes predicted from manufacturing simulations : Assessing the impact of the carbon-binder spatial location on the electrochemical performance, J. Power Sources. 444 (2019) 227285, doi:10.1016/j.jpowsour.2019.227285.

[50] B. Geveci, ParaView: An End-User Tool for Large Data Visualization ParaViewWeb View project, 836 (2005). https://www.researchgate.net/publication/247111133.

[51] F. Pouraghajan, H. Knight, M. Wray, B. Mazzeo, R. Subbaraman, J. Christensen, D. Wheeler, Quantifying Tortuosity of Porous Li-Ion Battery Electrodes: Comparing Polarization-Interrupt and Blocking-Electrolyte Methods, J. Electrochem. Soc. 165 (2018) A2644-A2653, doi:10.1149/2.0611811jes.

[52] J. Landesfeind, J. Hattendorff, A. Ehrl, W.A. Wall, H.A. Gasteiger, Tortuosity Determination of Battery Electrodes and Separators by Impedance Spectroscopy, J. Electrochem. Soc. 163 (2016) A1373-A1387, doi:10.1149/2.1141607jes.

[53] L.S. Kremer, A. Hoffmann, T. Danner, S. Hein, B. Prifling, D. Westhoff, C. Dreer, A. Latz, V. Schmidt, M. Wohlfahrt-Mehrens, Manufacturing Process for Improved Ultra-Thick Cathodes in High-Energy Lithium-Ion Batteries, Energy Technol. 8 (2020), doi:10.1002/ente.201900167.

[54] E.N. Primo, M. Chouchane, M. Touzin, P. Vasquez, A.A. Franco, Understanding the calendering processability of Li(Ni0.33Mn0.33Co0.33)O2-based cathodes, J. Power Sources. (2020).

[55] A. Torayev, A. Rucci, P.C.M.M. Magusin, A. Demortière, V. De Andrade, C.P. Grey, C. Merlet, A.A. Franco, Stochasticity of Pores Interconnectivity in Li-O2 Batteries and its Impact on the Variations in Electrochemical Performance, J. Phys. Chem. Lett. 9 (2018) 791–797, doi:10.1021/acs.jpclett.7b03315.

[56] A. Torayev, P.C.M.M. Magusin, C.P. Grey, C. Merlet, A.A. Franco, Importance of Incorporating Explicit 3D-Resolved Electrode Mesostructures in Li-O2 Battery Models, ACS Appl. Energy Mater. 1 (2018) 6433–6441, doi:10.1021/acsaem.8b01392.

[57] W.B. Hawley, J. Li, Electrode manufacturing for lithium-ion batteries—Analysis of current and next generation processing, J. Energy Storage. 25 (2019) 100862, doi:10.1016/j.est.2019.100862.

[58] A. Shodiev, E.N. Primo, M. Chouchane, T. Lombardo, A.C. Ngandjong, A. Rucci, A.A. Franco, 4D-resolved physical model for Electrochemical Impedance Spectroscopy of Li(Ni1-x-yMnxCoy)O2-based cathodes in symmetric cells: Consequences in tortuosity calculations, J. Power Sources. (2020) 227871, doi:10.1016/j.jpowsour.2020.227871.

[59] M.F. Lagadec, V. Wood, Microstructure of Celgard® PP1615 Lithium-Ion Battery Separator, (2018).

[60] M.F. Lagadec, M. Ebner, R. Zahn, V. Wood, Communication — Technique for Visualization and Quantification of Lithium-Ion Battery Separator Microstructure, 163 (2016) 992-994. 10.1149/2.0811606jes.

[61] H. Banda, S. Périé, B. Daffos, L. Dubois, O. Crosnier, P. Simon, P.L. Taberna, F. Duclairoir, Investigation of ion transport in chemically tuned pillared graphene materials through electrochemical impedance analysis, Electrochim. Acta. 296 (2019) 882–890, doi:10.1016/j.electacta.2018.11.122.

[62] Home | Artistic, (n.d.). https://www.erc-artistic.eu/ (accessed January 22, 2021).

[63] T. Danner, S. Eswara, V.P. Schulz, A. Latz, Characterization of gas diffusion electrodes for metal-air batteries, J. Power Sources. 324 (2016) 646–656, doi:10.1016/j.jpowsour.2016.05.108.